

# Markerless and Efficient 26-DOF Hand Pose Recovery

Iasonas Oikonomidis, Nikolaos Kyriazis, and Antonis A. Argyros

Institute of Computer Science, FORTH  
and  
Computer Science Department, University of Crete  
{oikonom,kyriazis,argyros}@ics.forth.gr  
<http://www.ics.forth.gr/cvrl/>

**Abstract.** We present a novel method that, given a sequence of synchronized views of a human hand, recovers its 3D position, orientation and full articulation parameters. The adopted hand model is based on properly selected and assembled 3D geometric primitives. Hypothesized configurations/poses of the hand model are projected to different camera views and image features such as edge maps and hand silhouettes are computed. An objective function is then used to quantify the discrepancy between the predicted and the actual, observed features. The recovery of the 3D hand pose amounts to estimating the parameters that minimize this objective function which is performed using Particle Swarm Optimization. All the basic components of the method (feature extraction, objective function evaluation, optimization process) are inherently parallel. Thus, a GPU-based implementation achieves a speedup of two orders of magnitude over the case of CPU processing. Extensive experimental results demonstrate qualitatively and quantitatively that accurate 3D pose recovery of a hand can be achieved robustly at a rate that greatly outperforms the current state of the art.

## 1 Introduction

The problem of effectively recovering the pose (3D position and orientation) of human body parts observed by one or more cameras is interesting because of its theoretical importance and its diverse applications. The human visual system exhibits a remarkable ability to infer the 3D body configurations of other humans. A wide range of applications such as human-computer interfaces, etc, can be built provided that this fundamental problem is robustly and efficiently solved [1]. Impressive motion capture systems that employ visual markers [2] or other specialized hardware have been developed. However, there is intense interest in developing markerless computer-vision based solutions, because they are non-invasive and, hopefully, cheaper than solutions based on other technologies (e.g., electromagnetic tracking).

The particular problem of 3D hand pose estimation is of special interest because by understanding the configuration of human hands we are in a position

to build systems that may interpret human activities and understand important aspects of the interaction of a human with her/his physical and social environment. Despite the significant amount of work in the field, the problem remains open and presents several theoretical and practical challenges due to a number of cascading issues. Fundamentally, the kinematics of the human hand is complicated. Complicated kinematics is hard to accurately represent and recover and also yields a search space of high dimensionality. Extended self-occlusions further complicate the problem by generating incomplete and/or ambiguous observations.

## 1.1 Related Work

A significant amount of literature has been devoted to the problem of pose recovery of articulated objects using visual input. Moeslund et al [1] provide a thorough review covering the general problem of visual human motion capture and analysis. The problems of recovering the pose of the human body and the human hand present similarities such as the tree-like connectivity and the size variability of the articulated parts. However, a human hand usually has consistent appearance statistics (skin color), whereas the appearance of humans is much more diverse because of clothing.

A variety of methods have been proposed to capture human hand motion. Erol et al [3] present a review of such methods. Based on the completeness of the output, they differentiate between partial and full pose estimation methods, further dividing the last class into appearance-based and model-based ones.

Appearance-based methods estimate hand configurations from images directly after having learnt the mapping from the image feature space to the hand configuration space [4, 5, 6, 7]. The mapping is highly nonlinear due to the variation of hand appearances under different views. Further difficulties are posed by the requirement for collecting large training data sets and the accuracy of pose estimation. On the positive side, appearance based methods are usually fast, require only a single camera and have been successfully employed for gesture recognition.

Model-based approaches employ a 2D or 3D hand model [8, 9, 10, 11]. In the case of 3D hand models the hand pose is estimated by matching the projection of the model to the observed image features. The task is then formulated as a search problem in a high dimensional configuration space, which induces a high computational cost. Important issues to be addressed by such methods include the efficient construction of realistic 3D hand models, the dimensionality reduction of the configuration space and the development of techniques for fast and reliable hand posture estimation.

This paper presents a novel, generative method that treats the 3D hand pose recovery problem as an optimization problem that is solved through Particle Swarm Optimization (PSO). Under the taxonomy of [3], the present work can be categorized as a full, model-based pose estimation method that employs a single hypothesis. The method may integrate observations from an arbitrary number of available views without requiring special markers. This is clearly demonstrated by our decision to consider all free problem parameters jointly and simultaneously.

As a direct consequence, contrary to the work of [10], our formulation of the problem allows for a clear and effortless treatment of self-occlusions. PSO has been already applied for human pose recovery in [12], however this is done in a hierarchical fashion in contrast to our joint optimization approach. Additionally, the method of [12] is not directly applicable to hand pose recovery because stronger occlusions must be handled given weaker observation cues.

Being generative, the approach explores an essentially infinite configuration space. Thus, the accuracy of estimated pose is not limited by the size and content of the employed database, as e.g. in [7]. To the best of our knowledge, this is the first work that demonstrates that PSO can be applied to the problem of 3D hand pose recovery and solve it accurately and robustly. This is demonstrated in sequences with highly complex hand articulation where the hand is observed from relatively distant views. Additionally, it is demonstrated that the careful selection of inherently data parallel method components permits the efficient, near real-time 3D hand pose estimation and gives rise to the fastest existing method for model-based hand pose recovery.

The rest of this paper is organized as follows. Section 2 describes in detail the proposed method. Section 3 presents results from an extensive quantitative and qualitative experimental evaluation of the proposed method. Finally, Sec. 4 summarizes the paper by drawing the most important conclusions of this work.

## 2 Methodology

The proposed method can be summarized as follows. Observations of a human hand are acquired from a static, pre-calibrated camera network. For each observation, skin color detection and edge detection are performed to extract reference features. A 3D model of a human hand is adopted that consists of a collection of parameterized geometric primitives. Hand poses are represented by a total of 27 parameters that redundantly encode the 26 degrees of freedom of the human hand. Given the hand model, poses which would reproduce the observations are hypothesized. For each of them, the corresponding skin and edge feature maps are generated and compared against their reference counterparts. The discrepancy between a given pose and the actual observation is quantified by an error function which is minimized through Particle Swarm Optimization (PSO). The pose for which this error function is minimal constitutes the output of the proposed method at a given moment in time. Temporal continuity in hand motion is assumed. Thus, the initial hypotheses for current time instance are restricted in the vicinity of the solution for the previous time instant. The method incorporates computationally expensive processes which cannot be adequately handled by conventional CPU processing. However, the exploitation of the inherent data parallelism of all the required components through a GPU powered implementation, results in near real-time computational performance. The following sections describe in more detail the components outlined above.

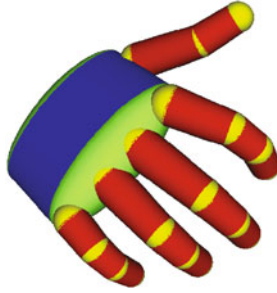


**Fig. 1.** Hand model with colored parts. Each color denotes a different type of geometric primitive (blue for elliptic cylinders, green for ellipsoids, yellow for spheres and red for cones).

## 2.1 Observation Model

The proposed hand pose recovery method operates on sequences of synchronized views acquired by intrinsically and extrinsically calibrated cameras. A set of images acquired from a set of such cameras at the same moment in time is called a *multiframe*. If  $M_i = \{I_1, I_2, \dots\}$  is a multiframe of a sequence  $S = \{M_1, M_2, \dots\}$  then  $I_j$  denotes the image from the  $j$ -th camera/view at the  $i$ -th time step. In the single camera case, a sequence of multiframe reduces to an image sequence.

An observation model similar to [10] is employed. For each image  $I$  of a multiframe  $M$ , an edge map  $o_e(I)$  is computed by means of Canny edge detection [13] and a skin color map  $o_s(I)$  is computed using the skin color detection method employed in [14]. As a convention, the label of 1 indicates presence and the label of 0 indicates the absence of skin or edges in the corresponding maps. For each edge map  $o_e(I)$ , a distance transform  $o_d(I)$  is computed. For each image  $I$ , maps  $O(I) = \{o_s(I), o_d(I)\}$  constitute its observation cues.

## 2.2 Hand Model

The model of hand kinematics used in this work is based on [15]. The kinematics of each finger, including the thumb, is modeled using four parameters encoding angles. More specifically, two are used for the base of the finger and two for the remaining joints. Bounds on the values of each parameter are set based on anatomical studies (see [15] and references therein). The global position of the hand is represented using a fixed point on the palm. The global orientation is parameterized using the redundant representation of quaternions. This parameterization results in a 26-DOF model encoded in a vector of 27 parameters.

The hand consists of a palm and five fingers. The palm is modeled as an ellipsoid cylinder and two ellipsoids for caps. Each finger consists of three cones and four spheres, except for the thumb which consists of two cones and three spheres (see Fig. 1). All required 3D shapes used in the adopted hand model consist of multiple instances of two basic geometric primitives, a sphere and a truncated cylinder. These geometric primitives, subjected to appropriate

homogeneous transformations, yield a model similar to that of [9]. Each transformation performs two different tasks. First, it appropriately transforms primitives to more general quadrics and, second, it applies the required kinematics. Using the shape transformation matrix

$$T_s = \begin{pmatrix} e \cdot s_x & 0 & 0 & 0 \\ 0 & e \cdot s_y & 0 & 0 \\ 0 & 0 & s_z & 0 \\ 0 & 0 & 1 - e & e \end{pmatrix}, \quad (1)$$

spheres can be transformed to ellipsoids and cylinders to elliptic cylinders or cones. In Eq.(1),  $s_x$ ,  $s_y$  and  $s_z$  are scaling factors along the respective axes. The parameter  $e$  is used only in the case of cones, representing the ratio of the small to the large radius of the cone before scaling (if not transforming to a cone,  $e$  is fixed to 1). Having a rigid transformation matrix  $T_k$  computed from the kinematics model, the final homogeneous transformation  $T$  for each primitive (sphere or cylinder) is

$$T = T_k \cdot T_s. \quad (2)$$

A non-trivial implementation issue (see Sec. 2.5) is the correct computation of surface normals. For given normals  $\vec{n}_i$  of the two primitives in use, and given homogeneous transformation  $T$ , the computation of the new surface normals  $\vec{n}_i'$  can be performed according to [16] using the equation  $\vec{n}_i' = (T^{-T})_{3 \times 3} \cdot \vec{n}_i$ .  $A_{3 \times 3}$  denotes the upper-left 3 by 3 submatrix of  $A$ .

Having a parametric 3D model of a hand, the goal is to estimate the model parameters that are most compatible to the observed images/image features (Sec. 2.1). To do so, we compute comparable image features from each hypothesized 3D hand pose (see Sec. 2.5). More specifically, given a hand pose hypothesis  $h$ , an edge map  $r_e(h)$  and a skin color map  $r_s(h)$  can be generated by means of rendering. The reference implementation of the rendering process is very similar to that of [9]. The informative comparison between each observation and corresponding hypotheses is detailed in Sec. 2.3.

### 2.3 Hypothesis Evaluation

The proposed method is based on a measure quantifying how compatible a given 3D hand pose is to the actual camera-based observations. More specifically, a distance measure between a hand pose hypothesis  $h$  and the observations of multiframe  $M$  needs to be established. This is performed by the computation of a function  $E(h, M)$  which measures the discrepancies between skin and edge maps computed in a multiframe and the skin and edge maps that are rendered for a given hand pose hypothesis:

$$E(h, M) = \sum_{I \in M} D(I, h, C(I)) + \lambda_k \cdot kc(h). \quad (3)$$

In Eq.(3),  $h$  is the hand pose hypothesis,  $M$  is the corresponding observation multiframe,  $I$  is an image in  $M$ ,  $C(I)$  is the set of camera calibration parameters

corresponding to image  $I$  and  $\lambda_k$  is a normalization factor. The function  $D$  of Eq.(3) is defined as

$$D(I, h, c) = \frac{\sum o_s(I) \otimes r_s(h, c)}{\sum o_s(I) + \sum r_s(h, c) + \epsilon} + \lambda \frac{\sum o_d(I) \cdot r_s(h, c)}{\sum r_e(h, c) + \epsilon}, \quad (4)$$

where  $o_s(I), o_d(I), r_s(h, c), r_e(h, c)$  are defined in Sec. 2.1. A small term  $\epsilon$  is added to the denominators of Eq.4) to avoid divisions by zero. The symbol  $\otimes$  denotes the logical XOR (exclusive disjunction) operator. Finally,  $\lambda$  is a constant normalization factor. The sums are computed over entire feature maps. The function  $kc$  adds a penalty to kinematically implausible hand configurations. Currently, only adjacent finger inter-penetration is penalized. Therefore,  $kc$  is defined as

$$kc(h) = \sum_{p \in \text{pairs}} \begin{cases} -\phi(p) & \phi(p) < 0 \\ 0 & \phi(p) \geq 0 \end{cases}, \quad (5)$$

where  $\text{pairs}$  denotes the three pairs of adjacent fingers, excluding the thumb, and  $\phi$  denotes the difference between the abduction-adduction angles of those fingers. In all experiments the values of  $\lambda$  and  $\lambda_k$  were both set to 10.

## 2.4 Particle Swarm Optimization

Particle Swarm Optimization (PSO) is an optimization technique that was introduced by Kennedy et al [17]. It is an evolutionary algorithm since it incorporates concepts such as populations, generations and rules of evolution for the atoms of the population (particles). A population is essentially a set of particles which lie in the parameter space of the objective function to be optimized. The particles evolve in runs which are called generations according to a policy which emulates “social interaction”.

Canonical PSO, the simplest of PSO variants, was preferred among other optimization techniques due to its simplicity and efficiency. More specifically, it only depends on very few parameters, does not require extra information on the objective function (e.g., its derivatives) and requires a relatively low number of evaluations of the objective function [18]. Following the notation introduced in [19], every particle holds its current position (current candidate solution, set of parameters) in a vector  $x_t$  and its current velocity in a vector  $v_t$ . Moreover, each particle  $i$  stores in vector  $p_i$  the position at which it achieved, up to the current generation  $t$ , the best value of the objective function. Finally, the swarm as a whole, stores in vector  $p_g$  the best position encountered across all particles of the swarm.  $p_g$  is broadcasted to the entire swarm, so that every particle is aware of the global optimum. The update equations that are applied in every generation  $t$  to reestimate each particle’s velocity and position are

$$v_t = K(v_{t-1} + c_1 r_1 (p_i - x_{t-1}) + c_2 r_2 (p_g - x_{t-1})) \quad (6)$$

and

$$x_t = x_{t-1} + v_t, \quad (7)$$

where  $K$  is a constant *constriction factor* [20]. In Eqs. (6),  $c_1$  is called the *cognitive component*,  $c_2$  is termed the *social component* and  $r_1, r_2$  are random samples of a uniform distribution in the range  $[0..1]$ . Finally,  $c_1 + c_2 > 4$  must hold [20]. In all performed experiments the values  $c_1 = 2.8$ ,  $c_2 = 1.3$  and  $K = \frac{2}{|2-\psi-\sqrt{\psi^2-4\psi}|}$  with  $\psi = c_1 + c_2$  were used.

Typically, the particles are initialized at random positions and their velocities to zero. Each dimension of the multidimensional parameter space is bounded in some range. If, during the position update, a velocity component forces the particle to move to a point outside the bounded search space, this component is zeroed and the particle does not perform any move at the corresponding dimension. This is the only constraint employed on velocities.

In this work, the search space is the 27-dimensional 3D hand pose parameter space, the objective function to be minimized is  $E(M, h)$  (see Eq.(3)) and the population is a set of candidate 3D hand poses hypothesized for a single multiframe. Thus the process of tracking a hand pose requires the solution of a sequence of optimization problems, one for each of the acquired multiframe. By exploiting temporal continuity, the solution over multiframe  $M_t$  is used to generate the initial population for the optimization problem of  $M_{t+1}$ . More specifically, the first member of the population  $h_{ref}$  for  $M_{t+1}$  is the solution for  $M_t$ ; The rest of the population consists of perturbations of  $h_{ref}$ . Since the variance of these perturbations depends on the image acquisition frame rate and the anticipated jerkiness of the observed hand motion, it has been experimentally determined in the reported experiments. The optimization for multiframe  $M_{t+1}$  is executed for a fixed amount of generations/iterations. After all generations have evolved, the best hypotheses  $h_{best}$  is dubbed as the solution for time step  $t + 1$ .

## 2.5 Exploiting Parallelism

A reference implementation of the proposed method was developed in MATLAB. A study of the computational requirements of the method components revealed that PSO and skin color detection are very fast. The computations of edge maps and their distance transforms are relatively slow but these tasks along with skin color detection are only executed once per multiframe. The identified computational bottlenecks are the rendering of a given 3D hand pose hypothesis and the subsequent evaluation of Eq.(3). More specifically, the hand model consists of a series of quadrics for which ray casting is used for rendering [9]. Additionally, since multiple quadrics overlap on the projection plane, pixel overwriting will occur and z-buffering is required so as to produce correct edge maps. The computation of Eq.(3) is a matter of pixel-wise multiplication and summation over entire images. The whole process is computationally expensive and prevents real-time performance. Reasonable PSO parameterizations where particles and generations range in the orders of tens, correspond to more than 4 minutes of processing time per multiframe.

GPU accelerated observation models have been employed in the past (e.g. [21]). In contrast to previous work, we provide a detailed description of a GPU implementation that exploits parallelism beyond the point of straightforward

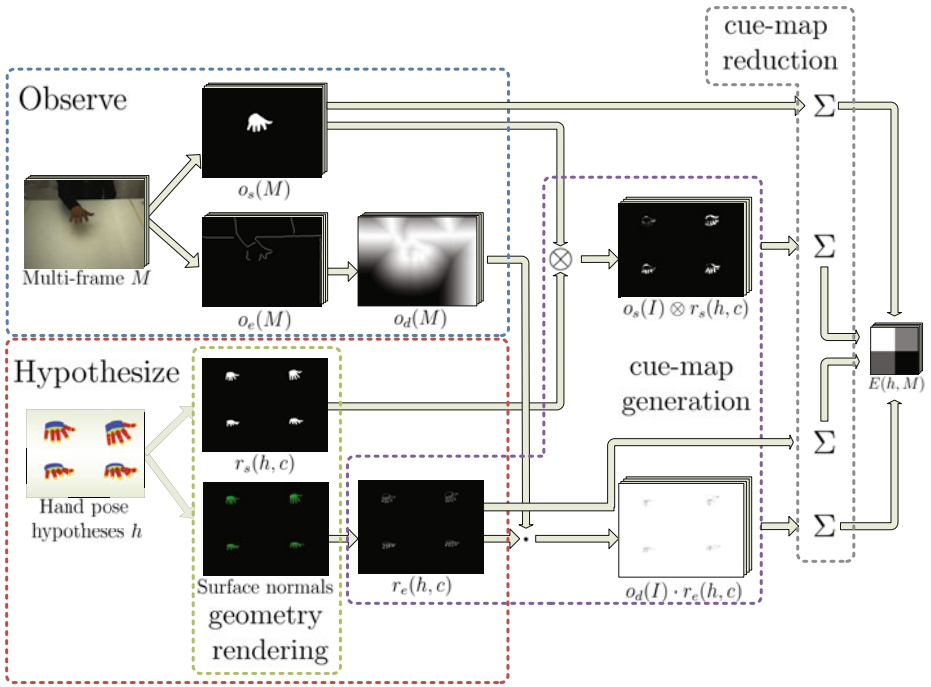


**Fig. 2.** Back-projection error computation flowchart. Observations of a human hand and hypothesized 3D poses are compared. Reference features are extracted from multiframe images by means of skin color detection and edge detection. Artificial features are generated for the 3D pose hypotheses by means of rendering and edge detection. The three main GPU steps are annotated: geometry rendering, cue-map generation and cue-map reduction.

image processing and rendering. Our GPU implementation targets the acceleration of the two performance bottlenecks, i.e., rendering and evaluation. The rest of the tasks are also susceptible to acceleration (e.g. [22, 23, 24]) but this was not considered in this work. The final implementation used the Direct3D rendering pipeline to accelerate the computationally demanding tasks and MATLAB to perform the rest of the tasks as well as overall task coordination.

Rendering and evaluation of Eq.(3) are decomposed in three major GPU computation steps: geometry rendering, cue-map generation and cue-map reduction (see Fig. 2). Multiple particles are evaluated in large batches instead of single particles. This design choice defines a fine parallelization granularity which makes GPUs the optimal accelerator candidate.

**Geometry rendering.** The goal of the geometry rendering step is to simultaneously render multiple hand hypotheses in a big tiled rendering. Multiple renderings, instead of sequences of single renderings, were preferred in order to maximally occupy the GPU cores with computational tasks. The non-trivial issues to address are geometry instancing and multi-viewport clipping.



Hardware instancing [24] is used to perform multiple render batches efficiently. Efficiency regards both optimal GPU power exploitation and minimal memory usage. Batch rendering of multiple hand configurations essentially amounts to rendering of multiple instances of spheres and cylinders. However, the respective geometric instantiations are not required to be explicit. Hardware geometry instancing can be used in order to virtually replicate reusable geometry and thus make instantiation implicit.

A specialized pixel shader is used in order to perform custom multi-viewport clipping. Multiple viewports are required to be simultaneously rendered. However, conventional rendering pipelines do not account for multiple viewports, except for the case of sequential renderings. Unless multi-viewport clipping was performed, out of bounds geometry would expand beyond the tiles and spoil adjacent renderings.

The information that is transferred from CPU to GPU are the projection matrices  $c$  for each tile and the view matrix  $T$  for each primitive. The output of this rendering is the map  $r_s(h, c)$ , per pixel depth and per pixel normal vectors, encoded in four floating point numbers.

**Cue-map generation.** During cue-map generation, the output of the geometry rendering step is post-processed in order to provide cue-maps  $r_s(h, c)$ ,  $r_e(h, c)$ ,  $o_s(I) \otimes r_s(h, c)$  and  $o_e(I) \cdot r_e(h, c)$  of Eq.(3). Cue-map  $r_s(h, c)$  passes through this stage since it is computed during geometry rendering (see Fig. 2). Cue-map  $r_e(h, c)$  is computed by thresholding the discontinuity in normal vectors for a cross-neighborhood around each pixel. Cue-maps  $o_s(I) \otimes r_s(h, c)$  and  $o_e(I) \cdot r_e(h, c)$  are trivially computed by element wise operations between the operands.

**Cue-map reduction.** In the cue-map reduction step, scale space pyramids are employed to efficiently accumulate values across tiles. The expected input is an image that encodes maps  $r_s(h, c)$ ,  $r_e(h, c)$ ,  $o_s(I) \otimes r_s(h, c)$  and  $o_e(I) \cdot r_e(h, c)$  and the expected output is the sum over logical tiles of these maps. The pyramids are computed by means of sub-sampling, which is a very efficient GPU computation. Once the sums have been accumulated, the computation of Eq.(3) is straightforward.

### 3 Experimental Evaluation

The quantitative and qualitative experimental validation of the proposed method was performed based on both synthetic and real-world sequences of multiframe.

#### 3.1 Quantitative Evaluation Based on Synthetic Data

The quantitative evaluation of the proposed method was based on synthetic sequences of multiframe which make possible the assessment of the proposed method against known ground truth. Towards this end, the hand model presented in Sec. 2.2 was animated so as to perform motions as simple as waving

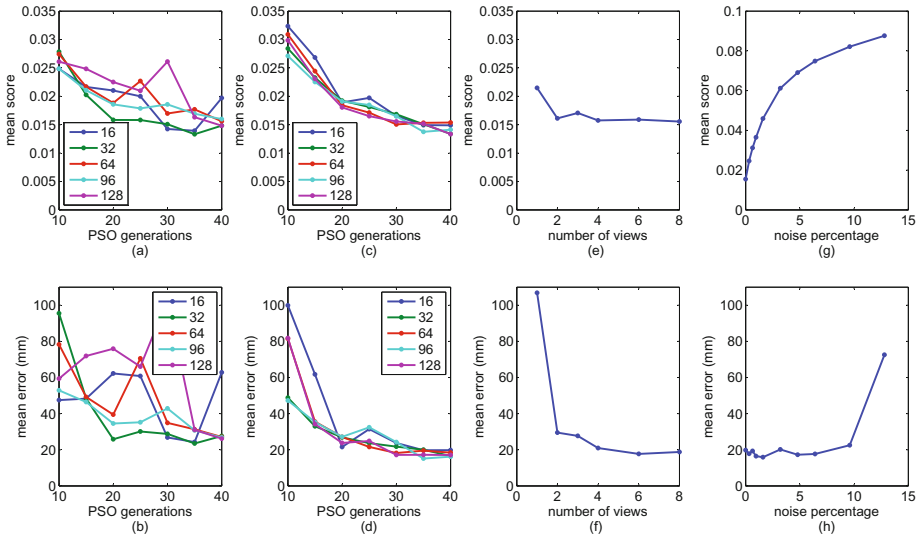


**Fig. 3.** Performance of the proposed method for different values of selected parameters. In the plots of the top row, the vertical axis represents the mean score  $E$ . In the plots of the bottom row, the vertical axis represents mean error in  $mm$  (see text for additional details). (a),(b): Varying values of PSO particles and generations for 2 views. (c),(d): Same as (a),(b) but for 8 views. (e),(f): Increasing number of views. (g),(h): Increasing amounts of noise.

and as complex as object grasping. A synthetic sequence of 360 poses of the moving hand was created. Each pose was observed by 8 virtual cameras surrounding the hand. This results in a sequence of 360 multiframe of 8 views, which constitute the input to the proposed method. The required cue maps were synthesized through rendering (see Sec. 2.2).

The performed quantitative evaluation assessed the influence of several factors such as PSO parameters, number of available views (i.e., multiframe size) and segmentation noise, over the performance of the proposed method. Figure 3 illustrates the obtained results. For each multiframe of the sequence, the best scoring hand pose  $h_{best}$  using the specified parameter values was found. Figures 3(a), (c), (e) and (g) provide plots of the score  $E(h_{best}, M)$  (averaged for all multiframe  $M$ ) as a function of various experimental conditions. Similarly, Figs. 3(b), (d), (f) and (h) illustrate the actual error in 3D hand pose recovery in millimeters, in the experimental conditions of Figs. 3(a), (c), (e) and (g), respectively. This error was computed as follows. The five fingertips as well as the center of the palm were selected as reference points. For each such reference point, the Euclidean distance between its estimated position and its ground truth position was first calculated. These distances were averaged across all multiframe, resulting in a single error value for the whole sequence.

Figures 3(a) and (b) show the behavior of the proposed method as a function of the number of PSO generations and particles per generation. In this

experiment, each multiframe consisted of 2 views with no noise contamination. It can be verified that varying the number of particles per generation does not affect considerably the error in 3D hand pose recovery. Thus, the number of generations appears to be more important than the number of particles per generation. Additionally, it can be verified that the accuracy gain for PSO parameterizations with more than 16 particles and more than 25 generations was insignificant. Figures 3(c), (d) are analogous to those of Figs 3(a),(b), except the fact that each multiframe consisted of 8 (rather than 2) views. The error variance is even smaller in this case as a consequence of the increased number of views which provides richer observations and, thus, more constraints. The accuracy gain for PSO parameterizations with more than 16 particles and more than 25 generations is even less significant.

In order to assess the behavior of the method with respect to the number of available views of the scene, experiments with varying number of views were conducted. Figures 3(e) and (f) show the behavior of the proposed method as a function of the size of a multiframe. For the experiments with less than 8 views, these were selected empirically so as to be as complementary as possible. More specifically, views with large baselines and viewing directions close to vertical were preferred. In these experiments, 128 PSO particles and 35 generations were used, and no segmentation noise was introduced in the rendered skin and edge maps. The obtained results (Figs. 3(e) and (f)) show that the performance improvement from one view to two views is significant. Adding more views improves the results noticeably but not significantly.

In order to assess the tolerance of the method to different levels of segmentation errors, all the rendered silhouette and edge maps were artificially corrupted with different levels of noise. The type of noise employed is similar to [7]. More specifically, positions are randomly selected within a map and the labels of all pixels in a circular neighborhood of a random radius are flipped. The aggregate measure of noise contamination is the percentage of pixels with swapped labels. In the plots of Figs. 3(g) and (h), the horizontal axis represents the percentage of noise-contaminated pixels in each skin map. Edge maps were contaminated with one third of this percentage. The contamination was applied independently to each artificial map  $r_s$  and  $r_e$ . In this experiment, 128 PSO particles and 35 PSO generations were used, and multiframe of eight views were considered. The plots indicate that the method exhibited robustness to moderate amounts of noise and failed for large amounts of noise. The exhibited robustness can be attributed to the large number of employed views. Since the noise of each view was assumed to be independent from all other views, the emerged consensus (over skin detection and edge detection) managed to cancel out low-variance noise. Figure 3 also demonstrates that the design choices regarding the objective function  $E$  (Sec. 2.3) are correct. This can be verified by the observed monotonic relation between  $E$  and the actual 3D hand pose estimation error.

Finally, Table 1 provides information on the runtime of these experiments. The table shows the number of multiframe per second for various parameterizations of the PSO (number of generations and number of particles per generation) and

**Table 1.** Number of multiframes per second processed for a number of PSO generations and camera views for 16/128 particles per generation

Generations	2 views	4 views	8 views
10	7.69/2.48	4.22/1.26	2.14/0.63
15	7.09/1.91	3.65/0.97	1.85/0.49
20	<b>6.23/1.55</b>	3.19/0.79	1.62/0.39
25	5.53/1.31	2.85/0.67	1.44/0.33
30	5.00/1.13	2.59/0.57	1.30/0.29
35	4.55/1.00	2.34/0.50	1.18/0.25
40	4.18/0.89	2.15/0.45	1.09/0.23

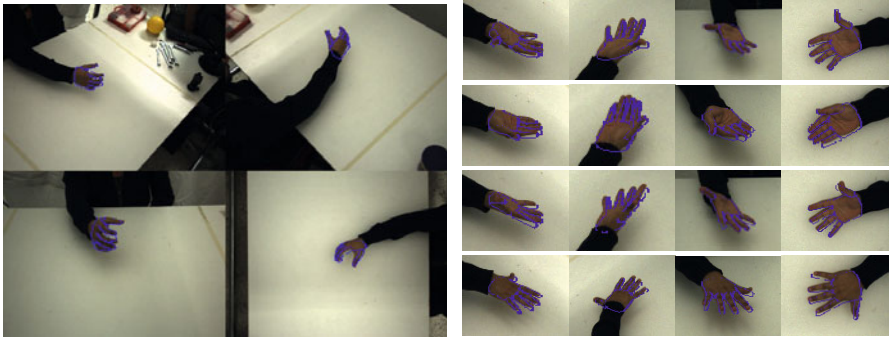


**Fig. 4.** Sample frames from real-world experiments. Left: four views of a multiframe of a cylindrical grasp. Right: Zoom on hands; Rows are from the same multiframe and columns correspond to the same camera view.

various number of views. The entry in boldface corresponds to 20 generations, 16 particles per generation and 2 views. According to the quantitative results presented earlier, this setup corresponds to the best trade-off between accuracy of results, computational performance and system complexity. This figure shows that the proposed method is capable of accurately and efficiently recovering the 3D pose of a hand observed from a stereo camera configuration at 6.2Hz. If 8 cameras are employed, the method delivers poses at a rate of 1.6Hz.

### 3.2 Experiments with Real World Images

Real-world image sequences were acquired using a multicamera system which is installed around a  $2 \times 1m^2$  bench and consists of 8 *Flea2* PointGrey cameras. Cameras are synchronized by a timestamp-based software that utilizes a dedicated *FireWire 2* interface (800 *MBits/sec*) which guarantees a maximum of 125  $\mu sec$  temporal discrepancy in images with the same timestamp. Each camera has a maximum framerate of 30 *fps* at highest (i.e.  $1280 \times 960$ ) image resolution. The workstation where images are gathered has a quad-core Intel i7 920 CPU, 6 GBs RAM and an Nvidia GTX 295 dual GPU with 894 *GFlops* processing power and 896 MBs memory per GPU core.

Several sequences of multiframe have been acquired, showing various types of hand activities such as isolated motions and hand-environment interactions including object grasping. Figure 4 provides indicative snapshots of 3D hand pose estimation superimposed on the original image data. Videos with results of these experiments are available online<sup>1</sup>.

## 4 Discussion

In this paper, we proposed a novel method for the visual recovery of 3D hand pose of a human hand. This is formulated as an optimization problem which is accurately and robustly solved through Particle Swarm Optimization. In an effort to propose a method that is both accurate and computationally efficient, appropriate design choices were made to select components that exhibit data parallelism which is exploited by a GPU based implementation. The experimental evaluation in challenging datasets (complex hand articulation, distant hand views) demonstrates that accurate pose recovery can be achieved at a framerate that greatly outperforms the current state of the art. The individual constituents of the proposed method are clearly separated. It is quite easy for changes to be made to the objective function, the optimization method or the hand model without affecting the other parts. Current research is focused on considering more compact search spaces through the use of dimensionality reduction techniques.

**Acknowledgements.** This work was partially supported by the IST-FP7-IP-215821 project GRASP. The contributions of Asimina Kazakidi and Thomas Sarmis (members of the CVRL/ICS/FORTH) are gratefully acknowledged.

## References

1. Moeslund, T.B., Hilton, A., Krüger, V.: A survey of advances in vision-based human motion capture and analysis. *CVIU* 104, 90–126 (2006)
2. Wang, R.Y., Popović, J.: Real-time hand-tracking with a color glove. *ACM Transactions on Graphics* 28, 1 (2009)
3. Erol, A., Bebis, G., Nicolescu, M., Boyle, R.D., Twombly, X.: Vision-based hand pose estimation: A review. *CVIU* 108, 52–73 (2007)
4. Athitsos, V., Sclaroff, S.: Estimating 3d hand pose from a cluttered image. In: *CVPR*, vol. 2, p. 432 (2003)
5. Rosales, R., Athitsos, V., Sigal, L., Sclaroff, S.: 3d hand pose reconstruction using specialized mappings. In: *ICCV*, pp. 378–385 (2001)
6. Wu, Y., Huang, T.S.: View-independent recognition of hand postures. In: *CVPR*, pp. 88–94 (2000)
7. Romero, J., Kjellstrom, H., Kragic, D.: Monocular real-time 3D articulated hand pose estimation. In: *IEEE-RAS Int'l Conf. on Humanoid Robots*, pp. 87–92 (2009)
8. Rehg, J.M., Kanade, T.: Visual tracking of high dof articulated structures: An application to human hand tracking. In: Eklundh, J.-O. (ed.) *ECCV 1994*. LNCS, vol. 801, pp. 35–46. Springer, Heidelberg (1994)

<sup>1</sup> <http://www.ics.forth.gr/~argyros/research/3Dhandpose.htm>

9. Stenger, B., Mendonca, P., Cipolla, R.: Model-based 3D tracking of an articulated hand. In: CVPR, pp. II-310-II-315 (2001)
10. Sudderth, E., Mandel, M., Freeman, W., Willsky, A.: Visual hand tracking using nonparametric belief propagation. In: CVPR Workshop, pp. 189-189 (2004)
11. de la Gorce, M., Paragios, N., Fleet, D.: Model-based hand tracking with texture, shading and self-occlusions. In: CVPR, pp. 1-8 (2008)
12. John, V., Trucco, E., Ivekovic, S.: Markerless human articulated tracking using hierarchical particle swarm optimisation. *Image and Vision Computing* 28, 1530-1547 (2010)
13. Canny, J.: A computational approach to edge detection. *PAMI* 8, 679-698 (1986)
14. Argyros, A., Lourakis, M.: Real-time tracking of multiple skin-colored objects with a possibly moving camera. In: Pajdla, T., Matas, J(G.) (eds.) ECCV 2004. LNCS, vol. 3023, pp. 368-379. Springer, Heidelberg (2004)
15. Albrecht, I., Haber, J., Seidel, H.: Construction and animation of anatomically based human hand models. In: 2003 ACM SIGGRAPH/Eurographics Symposium on Computer Animation, Eurographics Association, p. 109 (2003)
16. Turkowski, K.: Transformations of surface normal vectors. Technical report, Tech. Rep. 22, Apple Computer (July 1990)
17. Kennedy, J., Eberhart, R., Shi, Y.: *Swarm intelligence*. Morgan Kaufmann Publishers, San Francisco (2001)
18. Angeline, P.: Evolutionary optimization versus particle swarm optimization: Philosophy and performance differences. In: Porto, V.W., Waagen, D. (eds.) EP 1998. LNCS, vol. 1447, pp. 601-610. Springer, Heidelberg (1998)
19. White, B., Shaw, M.: Automatically tuning background subtraction parameters using particle swarm optimization. In: IEEE ICME, pp. 1826-1829 (2007)
20. Clerc, M., Kennedy, J.: The particle swarm - explosion, stability, and convergence in a multidimensional complex space. *IEEE Transactions on Evolutionary Computation* 6, 58-73 (2002)
21. Shaheen, M., Gall, J., Strzodka, R., Gool, L.V., Seidel, H.P.: A comparison of 3d model-based tracking approaches for human motion capture in uncontrolled environments. In: Workshop on Applications of Computer Vision, pp. 1-8 (2009)
22. Luo, Y., Duraiswami, R.: Canny edge detection on NVIDIA CUDA. In: CVPR 2008 Workshops, pp. 1-8 (2008)
23. Fischer, I., Gotsman, C.: Fast approximation of high-order Voronoi diagrams and distance transforms on the GPU. *Journal of Graphics, GPU, & Game Tools* 11, 39-60 (2006)
24. Pharr, M., Fernando, R.: *Gpu gems 2: programming techniques for high-performance graphics and general-purpose computation* (2005)